Energy & Environmental Science

ROYAL SOCIETY OF CHEMISTRY

PAPER

View Article Online
View Journal | View Issue

Cite this: *Energy Environ. Sci.*, 2025, **18**, 7504

A repulsive anode interface for high-energy and safe lithium metal batteries†

Jihoon Oh,[ab] Joseph L. Frank,[c] Randolph A. Leising,[c] Heejin Kim,[d] Jisub Kim,[ab] Minkwan Kim[ab] and Jang Wook Choi *[ab]

Received 15th March 2025,
Accepted 16th June 2025

DOI: 10.1039/d5ee01490e

rsc.li/ees

Metallic lithium (Li) anodes represent a tantalizing frontier in high-capacity battery design, yet their potential has long been undermined by catastrophic dendrite formation. Here, we exploit the extremely high interfacial energy between nanoscale tungsten (W) and Li to mitigate Li dendritic growth and promote compact grain formation to densify the Li metal deposits. By implementing an ultrathin 9 μm separator featuring dual W and boehmite (γ-AlO(OH)) coatings alongside a conventional carbonate electrolyte, Li metal batteries (LMBs) demonstrate exceptional performance: extended cyclability (78.9%@400cycles), fast-charging capabilities (6C, 18 mA cm^{-2}), and prolonged calendar life. Remarkably, the outstanding thermal stability prevents thermal runaway under abusive conditions (140 °C, 4.3 V). In practical fast-charge/slow-discharge scenarios (1.3C/0.3C), 2-stack pouch-cells operated under highly constrained conditions—limited Li metal (N/P ratio: 1.0) and lean electrolyte (E/C ratio: 2.2 g Ah^{-1})—achieved 82.2% capacity retention after 118 cycles. This study elucidates that interfacial energy control is the key to unlocking the full potential of Li metal anodes.

Broader context

Lithium metal batteries (LMBs) are widely recognized as a leading candidate for high-energy-density energy storage, offering substantial potential for deployment in electric vehicles and aerial mobility. However, their large-scale adoption faces significant obstacles due to their limited cycle and calendar lifespan, primarily caused by dendrite formation, uncontrolled interfacial reactions, and corrosion. While strategies like electrolyte optimization have been explored, commercial viability remains limited. Recognizing that Li degradation arises from interfacial instability and uneven deposition, we employ tungsten (W)—immiscible with Li—for interfacial engineering. This enhances Li cohesion within the grains, promoting dense, uniform Li deposition. A 30 nm-thick W interlayer notably improves the electrochemical performance under practical conditions (commercial N/P ratios, lean electrolyte), outperforming prior benchmarks. Additionally, our interfacial engineering strategy enhances thermal stability, effectively preventing thermal runaway, even under extreme scenarios such as full charge and prolonged exposure to 140 °C. By leveraging repulsive interfacial treatments, our work highlights the crucial role of interfacial energy control in making LMB technology viable.

Introduction

The global transition to electric vehicles (EVs) and aerial mobility has unleashed unprecedented demand for rechargeable batteries with higher energy density and enhanced safety.[1,2] While lithium-ion batteries (LIBs) with graphite anodes have dominated the market for decades due to their cost-effectiveness and cycling stability,[3,4] their performance is constrained by the theoretical capacity limits of graphite.[5,6] This limitation has catalyzed extensive research into next-generation anode materials with superior capacities, including silicon (Si),[7,8] lithium (Li) metal,[9,10] and even anode-less systems.[11,12] Among these, Li metal anodes have emerged as promising candidates owing to their ultrahigh theoretical capacity (3860 mA h g^{-1}) and lowest redox potential (−3.04 V *vs.* the standard hydrogen electrode).[13,14] However, the commercial adoption of Li metal anodes is hampered by critical challenges such as poor cycling stability and safety concerns, primarily due to dendrite formation during cycling, particularly under fast-charging conditions.[15,16]

Recent advancements in electrolyte engineering have shown potential to mitigate these challenges by suppressing dendritic growth and improving the overall performance of Li metal

[a] *School of Chemical and Biological Engineering and Institute of Chemical Process, Seoul National University, Seoul, Republic of Korea. E-mail: jangwookchoi@snu.ac.kr*
[b] *Hyundai Motor Group-Seoul National University (HMG-SNU) Joint Battery Research Center (JBRC), Seoul National University, Seoul, Republic of Korea*
[c] *SES AI Corporation, Woburn, MA, USA*
[d] *Division of Analytical Science, Korea Basic Science Institute, Daejeon, Republic of Korea*

† Electronic supplementary information (ESI) available. See DOI: https://doi.org/10.1039/d5ee01490e

batteries (LMBs).[17,18] Nevertheless, many proposed solutions rely on complex electrolyte formulations or require multiple additives and salts, all of which complicate the scalability and cost-effectiveness.[19–21] Other strategies, such as protective layer engineering, have emerged as alternative approaches.[22–24] These methods often incorporate lithiophilic seeds to promote uniform Li deposition through thermodynamically favorable alloy formation.[25–28] Despite these advances, achieving long-term cycling stability and scalable manufacturing processes remains a significant hurdle for commercialization.

Herein, we introduce a novel interfacial engineering approach to address the fundamental challenges of LMBs by enhancing the cohesion of the Li metal deposition layer and consequently mitigating dendritic growth. Our strategy is rooted in the principle of lithiophobicity[29]—the tendency of materials to repel Li metal—by selecting materials with minimal reactivity toward Li, as guided by phase-diagrams. Among the potential candidates, tungsten (W) has emerged as an optimal choice due to its exceptionally high interfacial energy against Li. Using an established physical vapor deposition (PVD) process, we deposited an ultrathin (30 nm) W layer onto a conventional polyethylene (PE) separator to form W-coated PE (W-PE), which promotes densely packed Li grains and minimizes parasitic reactions during cycling.

The effectiveness of our approach is corroborated by outstanding performance metrics: our dual-coated separator system, which incorporates 30 nm-thick W and 2 μm-thick boehmite (γ-AlO(OH)) layers with a total thickness of only 9 μm, enabled LMBs to realize exceptional cycling stability (78.9% capacity retention after 400 cycles), superior fast-charging capabilities (up to the 6C rate at 18 mA cm^{-2}), and extended calendar life. These improvements stem from the smaller surface area occupied by the Li metal deposits, facilitated by Li densification induced by our repulsive W coating. Notably, these results were realized with a conventional carbonate-based electrolyte, challenging the longstanding belief that complex electrolyte chemistries are indispensable for high-performance LMBs.

The W-PE also demonstrated remarkable thermal stability by effectively preventing thermal runaway under abusive conditions, thereby addressing a critical safety concern in advanced battery technology.[30,31] Most significantly, in practical fast-charge/slow-discharge testing (1.3C/0.3C) using 2-stack pouch-cells under commercially relevant conditions—including limited Li metal (N/P ratio of 1.0) and a lean electrolyte (E/C ratio of 2.2 g A h^{-1})—the cells retained 82.2% capacity over 118 cycles, which represents notable LMB performance under such stringent conditions. These achievements mark a significant advancement toward practical LMB technology and provide a scalable pathway to overcome the persistent challenges associated with Li metal anodes.

Results and discussion

W coating with extremely high Li interfacial energies

Li metal anodes typically develop dendritic and irregular morphologies during cycling,[32] with this large-surface-area growth accelerating unwanted side reactions with the electrolyte. Moreover, the calendar life of these cells is severely limited by corrosion reactions during idle periods, a significant barrier to industrial implementation of LMBs.[33–36] Our aim was to promote compact and dense Li growth *via* interfacial repulsive forces, achievable by introducing lithiophobic materials at the anode interface (Fig. 1a).

The concept of lithiophobicity parallels that of hydrophobicity, where liquids maintain large contact angles and spherical geometry without surface wetting. Similarly, Li in contact with lithiophobic surfaces exhibits large contact angles and the desired densification.[37] We selected W as our lithiophobic coating material due to its intrinsic immiscibility with Li, based on the binary phase information (Table S1, ESI†).[38] Density functional theory (DFT) calculations confirmed the absence of mixing phases between W and Li across the temperature range 0–500 K (Fig. 1b). The mixing enthalpy, calculated *via* both DFT (Fig. 1c) and cluster expansion fitting (Fig. 1d), approaches 1.0 eV per atom, indicating strong intermetallic repulsion. This repulsive interaction serves as the driving force for promoting dense Li plating through enhanced contact angles at the W-Li interface.

To quantify the inter-material repulsion, we calculated the interfacial energies between the relevant components. Given that both W and Li crystallize in body-centered cubic (bcc) structures, we modeled their interface using matched crystallographic facets (Fig. 1e). DFT revealed that W exhibits approximately threefold higher Li interfacial energies compared to lithium fluoride (LiF) (Fig. 1f, g and Fig. S1, ESI†), a prominent solid electrolyte interphase (SEI) component. Among SEI constituents, LiF demonstrates the highest Li interfacial energy,[39] making it particularly beneficial for stable interfaces in Li metal anodes. While considerable research has focused on developing LiF-rich SEI layers,[40,41] our W coating strategy establishes a design principle for interfacial engineering that achieves superior Li metal cohesion *via* a uniform, nanoscale repulsive layer.

W metal was deposited on conventional PE separators using a facile metal sputtering process. The processed surface exhibited the characteristic silver coloration of W, confirming successful deposition (Fig. 2a and Fig. S2, ESI†). The unaltered appearance of the opposite surface demonstrates selective and uniform deposition of the ultrathin layer on one side of the separator (Fig. S3, ESI†). Time-of-flight secondary ion mass spectrometry (ToF-SIMS) analysis verified the precise coating thickness of 30 nm (Fig. 2b and c). 180° peel-off tests demonstrated comparable adhesion strengths before and after the W coating, confirming strong adhesion between the coating layer and the separator substrate (Fig. S4, ESI†).

This nanoscale W coating offers several advantages over conventional protective layer designs. The thin-film sputtering technique enables large-scale, uniform fabrication while minimally increasing the thickness, thereby preserving the energy density of the cell. Along this direction, a roll-to-roll sputtering process can be considered for seamless integration with existing LIB manufacturing processes. Atomic force microscopy (AFM) analysis revealed negligible changes in the surface roughness after coating (Fig. S5 and Table S2, ESI†). Additionally, the ultrathin coating retains the essential properties of the separator,

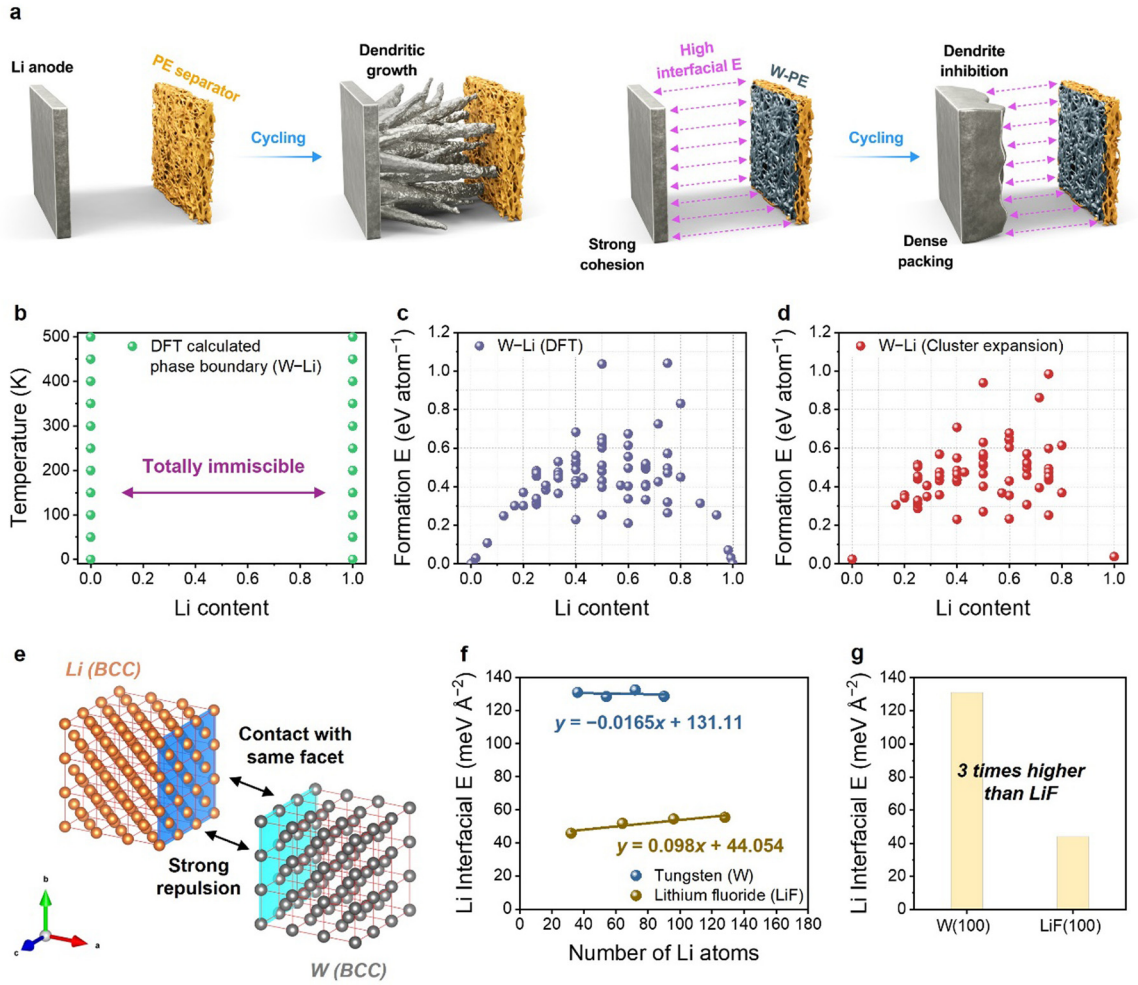

Fig. 1 DFT calculations of W metals. (a) Graphical depiction of the W coating on the separator to promote densification of the Li metal deposition layer. (b)–(g) DFT calculations of the W metal. (b) Phase boundary between W and Li. Formation energy of the W-Li alloy obtained from (c) DFT calculations and (d) cluster expansion fitting. (e) Atomic model illustrating the interfacial contact between W and Li. (f) and (g) Calculated Li interfacial energies for W and LiF.

including uninterrupted Li-ion pathways and compatibility with diverse electrolyte and protective layer strategies. Measurements confirmed that air permeation and the electrical conductivity remained essentially unchanged after coating (Fig. 2d and Fig. S6, ESI†). Li-ion transport was similarly unaffected, as evidenced by minimal changes in both ionic conductivity and Li^+ transference number (Fig. S7, ESI†).

Contact angle measurements with a carbonate-based electrolyte revealed decreased angles on the W-PE compared to the uncoated PE (Fig. 2e and f). To verify the lithiophobic properties of the W coating, we conducted molten Li contact angle experiments by placing molten Li on the W surface (Fig. 2g). The observed contact angle of 143° indicates complete non-wetting behavior, which promotes molten Li cohesion into a spherical geometry. This clarifies the critical role of high interfacial energy in the densification of the Li metal deposition layer.

Electrochemical analyses were performed using Li–Li symmetric and Li–Cu asymmetric cells with a commercial carbonate electrolyte: 1 M $LiPF_6$ in EC/DEC with 10% FEC. Given that these evaluations involve Li metal deposition on both sides, a 30 nm-thick W coating was uniformly applied to both sides of the separator. At a current density of 1 mA cm^{-2} and capacity of 1 mA h cm^{-2}, the Li–Li symmetric cell with the W-PE operated for 3500 hours without internal short circuits or significant overpotential increases, whereas the cell with the uncoated PE operated for only 350 hours before its overpotential increased drastically (Fig. 2h). The performance at higher current densities (6 and 9 mA cm^{-2}) and capacity (3 mA h cm^{-2}) was similar (Fig. S8, ESI†).

The cycling stability of Li–Cu asymmetric cells was evaluated at 1 mA cm^{-2} with a stripping voltage cutoff of 0.5 V (Fig. 2i and Fig. S9, ESI†). The cell with the uncoated PE had poor CE and its overpotential increased after 200 cycles. In contrast, the W-PE cell operated stably for 1000 cycles without short-circuiting while maintaining high CE. This performance substantially exceeds that of previously reported Li–Cu asymmetric cells using conventional carbonate electrolytes.[42,43]

The impact of the high interfacial energy of W was investigated by conducting comparative studies using silver (Ag)- and

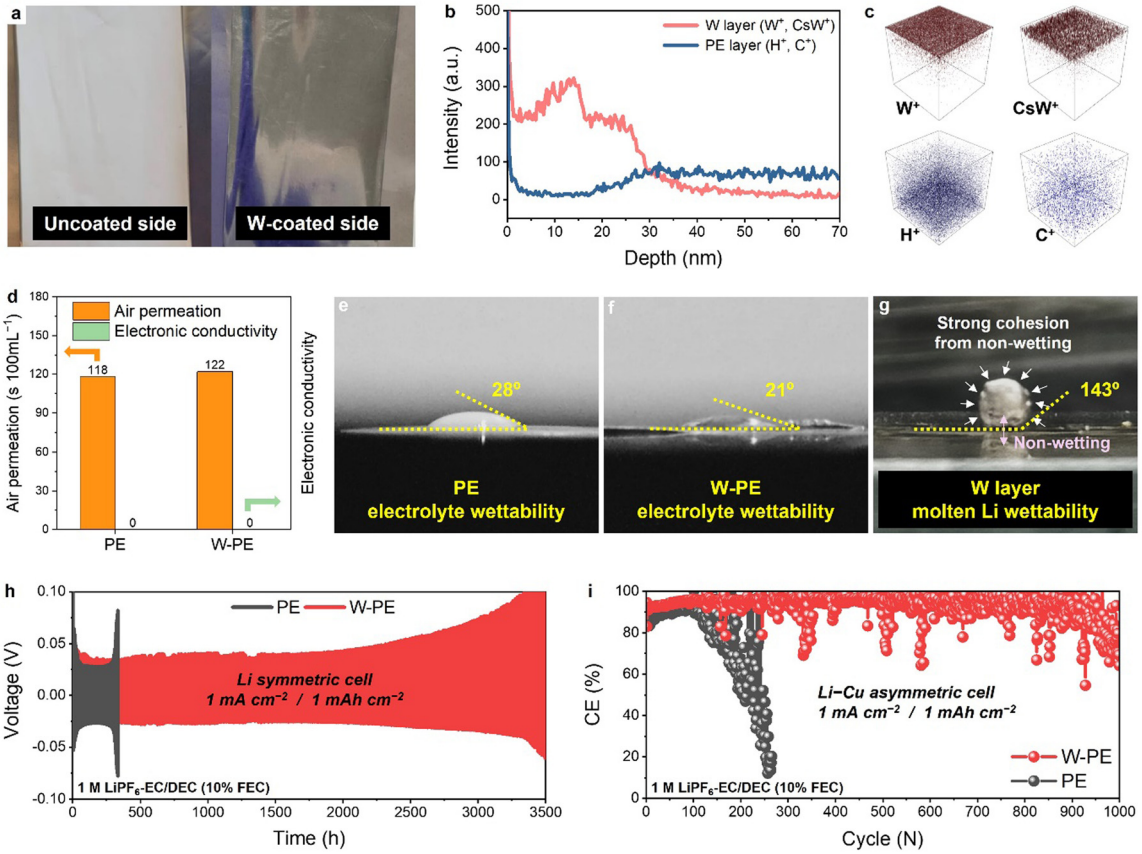

Fig. 2 Analysis and electrochemical evaluations of the W-PE. (a) Photographs of the uncoated PE and W-PE. (b) and (c) ToF-SIMS analysis, showing (b) depth profiles and (c) 3D elemental rendering images of the W-PE. (d) Measurements of air permeation and electronic conductivity. (e)–(g) Wettability evaluation: (e) and (f) with electrolyte and (g) with molten Li metal. (h) and (i) Cycling performance in (h) Li–Li symmetric cells and (i) Li–Cu asymmetric cells, using a carbonate-based electrolyte (1 M Li hexafluorophosphate ($LiPF_6$) in ethylene carbonate (EC)/diethyl carbonate (DEC) with 10% fluoroethylene carbonate (FEC)).

titanium (Ti)-coated separators. Ti, similar to W, is a lithiophobic metal that does not form alloys with Li, as confirmed by its phase diagram. DFT calculations revealed the interfacial energy of Ti with the Li (100) facet to be 66.799 meV $Å^{-2}$, roughly half that of W (Fig. S10a, ESI†). The Ti-PE demonstrated an improved cell lifespan of 800 hours compared to the uncoated PE, confirming the beneficial effects of Ti lithiophobicity (Fig. S10b, ESI†). Despite its lower interfacial energy compared to W, the higher interfacial energy of Ti than that of LiF supports its ability to stabilize Li metal anodes.

In contrast, the Ag-PE behaved differently. As a lithiophilic metal, Ag demonstrates strong Li affinity and lowers the Li deposition overpotential.[44,45] However, because its operational lifespan was limited to 550 hours, it underperformed compared to the Ti-PE (Fig. S11, ESI†). SEM analysis after Li electrodeposition revealed that Ti-PE facilitates considerably more homogeneous morphologies of Li deposits compared to Ag-PE counterparts (Fig. S12, ESI†). These results demonstrate that lithiophobic materials are more effective than lithiophilic materials for interfacial strategies aimed at regulating the Li metal deposition morphology, as their repulsive forces promote spontaneous Li metal cohesion. DFT-calculated Li interfacial energies correlate directly with cycle life data from Li–Li symmetric cells (Table S3, ESI†).

The short-circuit behavior at high current densities was studied by evaluating Li–Li symmetrical cells by incrementally increasing and subsequently decreasing the current density (Fig. S13 and S14, ESI†). The cell with the uncoated PE exhibited significant voltage noise at high current densities and displayed characteristic soft short-circuit behavior, manifested as a flat voltage profile and lower overpotential upon returning to 1 mA cm^{-2}. In contrast, the cell with the W-PE, which maintained stable operation without voltage noise even at 10 mA cm^{-2}, preserved its consistent overpotential and voltage slope profiles when returned to 1 mA cm^{-2}. These behaviors demonstrated the effectiveness of the W coating to prevent short circuits under high current operation.

Chronopotentiometry was used in combination with *in situ* electrochemical impedance spectroscopy (EIS) to verify the short-circuit behavior and determine the respective resistance values. EIS measurements were recorded hourly during single-direction galvanostatic cycling of Li–Li symmetric cells at a current density of 1 mA cm^{-2} (Fig. S15, ESI†). The resistance of the cell with the uncoated PE decreased progressively, whereas the W-PE cell maintained stable resistance profiles. Internal short-circuiting is accompanied by the development of enhanced electron transfer pathways through the separator (Fig. S16, ESI†)[46] to significantly lower both the bulk resistance (R_{bulk})

and charge transfer resistance (R_{CT}).[47] These decreases serve as direct evidence of incipient short circuits. Furthermore, measurements during rest periods revealed that the open-circuit voltage (OCV) of the PE-based cell consistently approximated 0 V contrary to the W-PE cell (Fig. S17, ESI†) to further substantiate the soft short-circuit behavior of the former.

Densification of the Li metal anode

We used scanning electron microscopy (SEM) to analyze the morphology after Li deposition in symmetrical cells (current density: 3 mA cm^{-2}; capacity: 3 mA h cm^{-2}; Fig. 3a–f). In the PE-based cell, Li was deposited inhomogeneously on the existing Li metal and formed distinct surface islands with filamentous morphologies. In contrast, Li deposits in the W-PE cell were uniform, with indistinguishable separation between deposited and pre-existing Li. Cross-sectional SEM analysis further revealed thick and uneven Li deposition in the PE-based cell (Fig. 3c), whereas in the W-PE cell, Li deposits were densified throughout their cross section (Fig. 3f).

These morphological differences became more pronounced at an elevated current density of 6 mA cm^{-2} (Fig. S18, ESI†). Similar morphological distinctions were observed on stripped Li metal surfaces (Fig. S19, ESI†), with the PE-based cell showing significant void formation upon Li stripping, indicating that repeated plating-stripping cycles resulted in progressively severe dendritic growth. In contrast, void formation in the W-PE was greatly suppressed during stripping, demonstrating that the repulsive forces of W enhance the Li morphological stability not only during plating but also throughout the stripping processes.

Li metal densification during extended cycling with the W coating was analyzed using X-ray microscopy (XRM) coupled with micro-computed tomography (μCT) after 100 plating-stripping cycles at 1 mA cm^{-2} and 1 mA h cm^{-2} in Li–Li symmetrical cells. Following cell disassembly, iterative rotation and X-ray imaging enabled high-resolution 3D reconstruction (Fig. 3g). Unlike the cell with the uncoated PE (Fig. 3h), the W-PE cell developed dense Li grains resembling wood rings (Fig. 3i). Notably, this densification extended beyond the surface with the separator to penetrate and spread throughout the Li metal interior, as confirmed by 2D images of the horizontal mid-sections. These morphological features of Li deposits in the W-PE cell once again attest to the high W-Li interfacial energy that induced strong Li cohesion throughout the entire structure, consistent with the molten Li wettability observations (Fig. 2g). XRM analysis of the post-cycling separators provided additional insights (Fig. S20, ESI†). The uncoated PE experienced extensive Li dendrite penetration, evidenced by the dark contrasting regions corresponding to Li metal within the PE matrix. The W-PE exhibited no such contrasting, confirming that the W coating effectively prevented dendrite penetration.

Full-cell evaluations with a dual-coated 9 μm-thick ultrathin separator

We evaluated Li metal-based full-cells using $LiNi_{0.8}Co_{0.1}Mn_{0.1}O_2$ (NCM811) as the cathode material. For these cells, we applied the W coating (30 nm) exclusively to the anode-facing separator side, while coating the cathode-facing side with 2 μm-thick boehmite (γ-AlO(OH)) (Fig. 4a–c), which serves to enhance the mechanical and thermal stabilities of the separator.[48] The total separator thickness was only 9 μm to maintain a compact cell design for high energy density. Compared to its uncoated PE counterpart, the cell incorporating the W-PE demonstrated superior initial performance with improved reversible capacity and ICE during the formation cycle at 0.1C (Fig. S21, ESI†).

Rate capability tests under strict cutoff protocols during charge revealed the significant advantages of the W interfacial treatment (Fig. 4d). The performance disparity, which intensified at higher C-rates, highlighted the effectiveness of the W coating during fast charging. For example, at 6C (10-minute charge), the W-PE cell achieved 110 mA h g^{-1} reversible capacity, whereas that of the uncoated PE cell was negligible due to its severe overpotential. To isolate the W interface contribution, rate performance was further evaluated using a boehmite-only coated PE separator, which matched the uncoated PE performance, confirming that the observed enhancement in the rate performance stems mainly from the W interface (Fig. S22, ESI†). Significantly, under 3C (dis)charging conditions (20-minute charge), the PE and W-PE cells retained 43.6 mA h g^{-1} and 141.3 mA h g^{-1} after 150 cycles, respectively (Fig. 4e–g). Voltage profiles revealed slower overpotential increases in the W-PE cell during cycling, whereas the uncoated PE cell predominantly charged in the constant voltage (CV) region due to high overpotential buildup. These comparative results remind us of the challenge of achieving long-term cyclability under fast-charging conditions.

To evaluate the storage characteristics, we implemented an 8-hour rest protocol following charging to 4.3 V (Fig. 4h). This protocol specifically probes the corrosiveness of the Li metal anode during electrochemically inactive periods, and provides critical insights into the calendar life, essential for practical battery applications. During 0.5C cycling (Fig. 4i), the W-PE cell retained 78.9% of its capacity over 400 cycles with exceptional durability even under the 8-hour rest protocol with a standard carbonate electrolyte. In contrast, the uncoated PE experienced early capacity loss due to electrolyte depletion. These results underscore the significant impact of repulsive interfacial engineering on Li metal anode densification with corrosion mitigation. Incidentally, the conventional carbonate electrolytes used in these experiments demonstrate the feasibility of utilizing established electrolyte options while highlighting the potential for further improvement in the cyclability by employing recently developed new electrolyte chemistries.[18,49–52]

Cycling under practical scenarios

We conducted pouch-cell evaluations with limited Li metal and electrolyte resources to assess the practical viability of our approach (Fig. 5). While these resource limitations can drive advancements in cost reduction and energy density,[53,54] they significantly compromise cycling performance—a critical challenge in LMBs. With single-stack 36 mA h pouch-cells (Fig. 5a–c) and a conventional carbonate-based electrolyte without complex

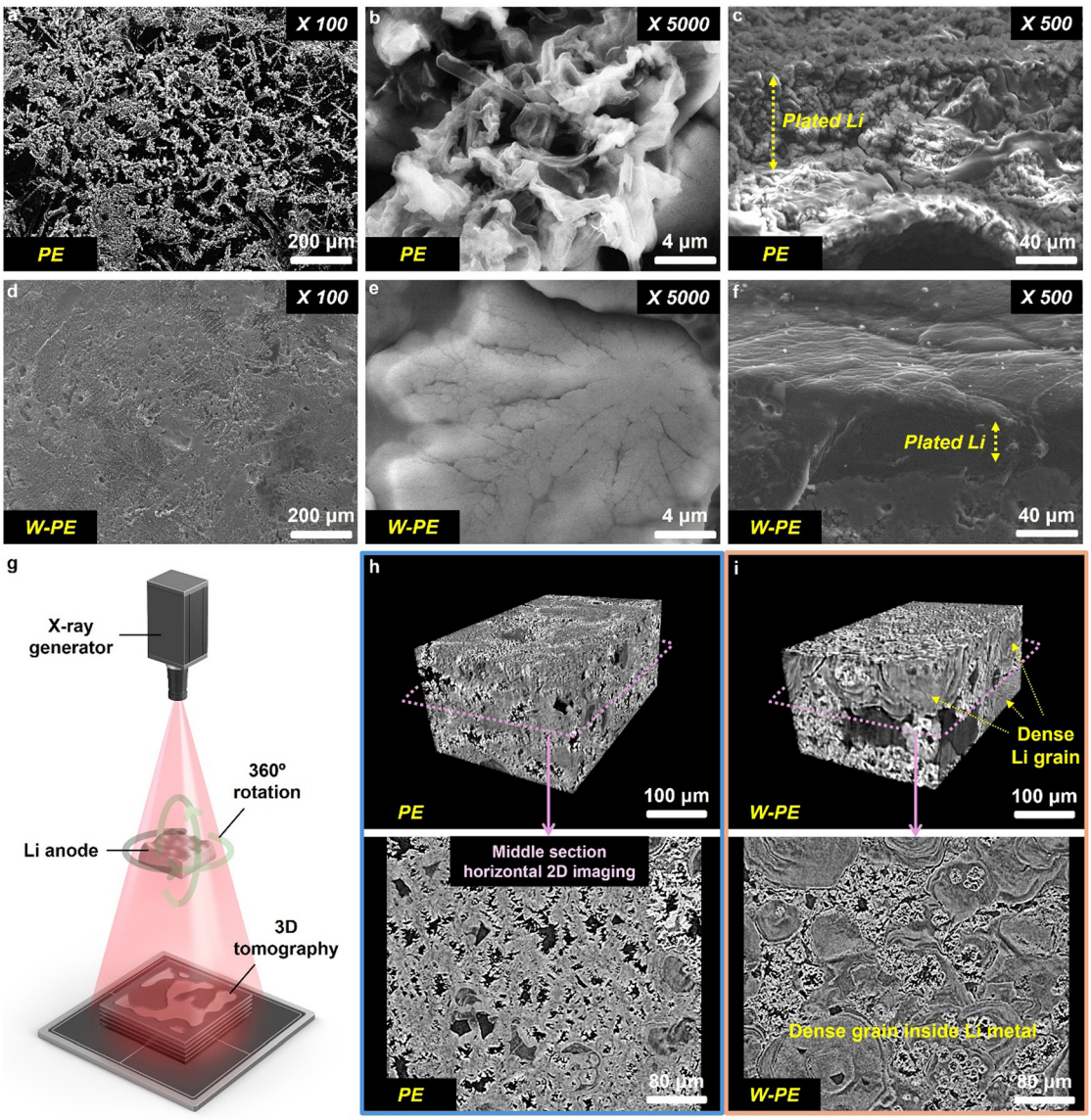

Fig. 3 Post-cycling morphology analysis of Li metal anodes. (a)–(f) SEM images of Li metal anodes after the 1st plating. With PE: (a) and (b) surface SEM images and (c) cross-sectional SEM image. With W-PE: (d) and (e) surface SEM images and (f) cross-sectional SEM image. (g) Schematic illustration of X-ray tomography for post-cycling Li metal anodes. (h) and (i) XRM 3D and 2D renderings of Li metal anodes with (h) PE and (i) W-PE after 100 cycles.

electrolyte processing, the W-PE cell retained 94.1% of its capacity over 100 cycles. In contrast, the capacity of the cell with uncoated PE rapidly decayed after only 20 cycles.

SES AI Corporation further validated the effect of W-PE by testing the 2-stack 118-mA h pouch-cells under more stringent practical fast-charge (1.3C) and slow-discharge (0.3C) conditions (N/P ratio: 1.0, E/C ratio: 2.2) (Fig. 5d–i). This challenging protocol, while representative of real-world scenarios, is not commonly used in LMB studies, because the Li metal anodes become more susceptible to dendritic growth under such asymmetric charge–discharge cycling.[55] To maximize the performance, an advanced electrolyte formulation consisting of 2 M LiFSI in 1,1,1-trifluoro-2,3-dimethoxypropane (TFDMP) was employed.[56] Even under these demanding conditions, the W-PE cell exhibited 82.2% capacity retention over 118 cycles without short-circuiting. Three independent cells demonstrated similar performance and reproducibility (Fig. 5f).

The non-uniform Li growth and rapid short-circuiting can be detected through charge capacity increase (CCI) analysis, as defined in Fig. 5g. Since elevated CCI values are reflective of the presence of Li in unintended locations (*e.g.*, dendrites penetrating the separator), CCI values exceeding 102% are indicative of failure due to internal short circuits. The pouch-cell with the uncoated PE experienced CCI failure within 20 cycles, whereas CCI failures of the W-PE cell only occurred once the capacity retention reached 80% across all three individual cells (Fig. 5h). The average CCI values and number of cycles at 80% capacity retention (Fig. 5i) reproducibly demonstrate the superior performance of W-PE. These evaluations confirmed the effectiveness of this repulsive interfacial engineering under practical

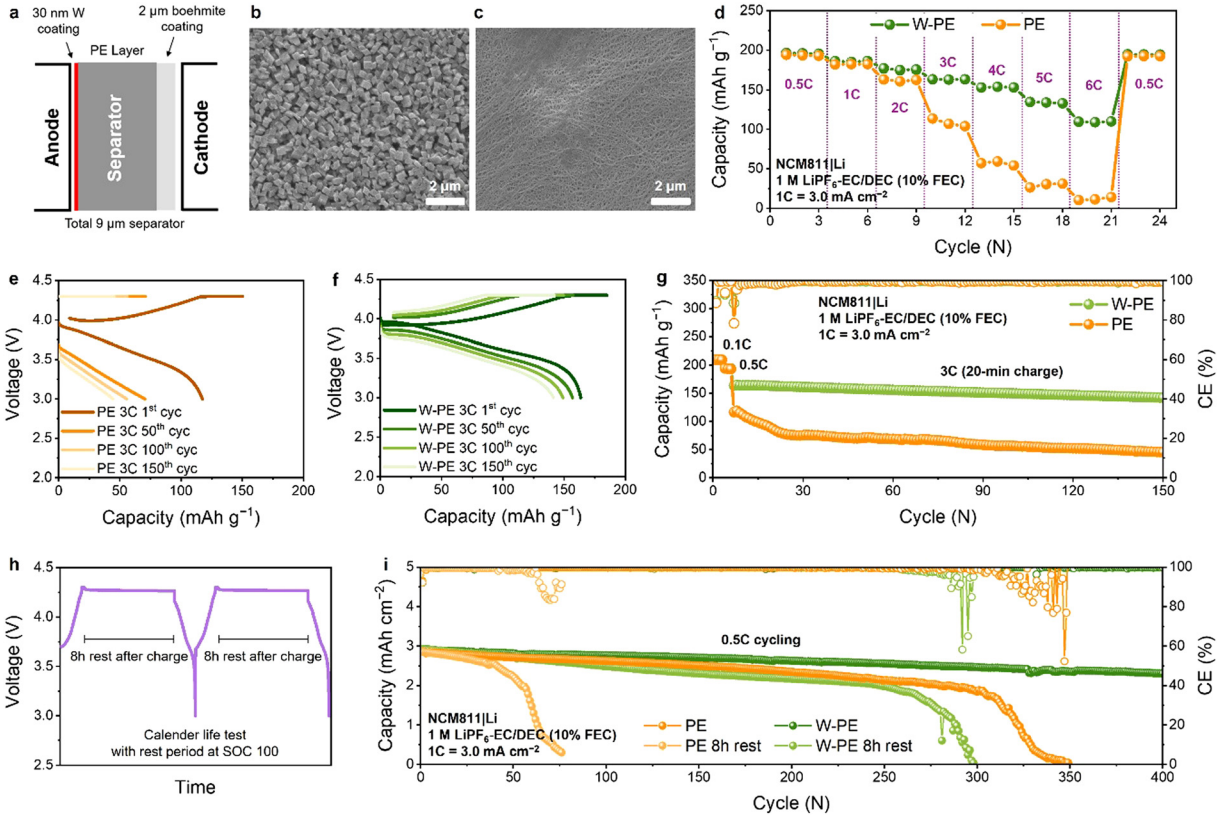

Fig. 4 Full-cell evaluations with a conventional carbonate-based electrolyte (1 M $LiPF_6$ in EC/DEC with 10% FEC). (a) Illustration of the W and boehmite dual-coating on the separator, with a total thickness of 9 μm. During cycling, the W layer faced the Li metal anode, whereas the boehmite layer faced the cathode. (b) and (c) Surface SEM images of (b) the boehmite-coated side and (c) the W-coated side. (d) Rate capability test results (1C = 3.0 mA cm^{-2}). (e)–(g) Fast-(dis)charging performance at 3C with a 20-minute charge time cutoff. Voltage profiles with the (e) PE and (f) W-PE, and (g) the corresponding cycling performances. (h) and (i) Calendar life evaluation to test corrosiveness. (h) Illustration of the rest periods at 100% SOC for 8 hours and (i) cycling performances with and without the rest periods.

conditions (fast-charge/slow-discharge, limited resources), thereby validating its industrial viability.

Among studies of LMBs with limited resources (thin Li and lean electrolyte)[57–63] (Fig. S23, ESI†), our solution uniquely delivers stable performance at high charging rates greater than 1C. Many of the previous studies primarily employed low charging and high discharging rates, which give rise to favorable Li metal morphology.[21,64] However, such protocols significantly deviate from practical operational requirements. Our repulsive interface strategy effectively accommodates these real-world conditions, highlighting its potential to bridge the gap between laboratory research and the commercial implementation of LMBs.

Enhanced safety against thermal runaway

Thermal runaway suppression tests (Fig. 6) were conducted to evaluate the thermal stability of the coated separator. The thermal abuse protocol adopted in this investigation entailed keeping the cells at 140 °C in the charged state at 4.3 V. The pouch-cell with the W-PE maintained its original cell temperature and voltage without internal short circuits or thermal runaway for 100 minutes (Fig. 6a), whereas, within 16 minutes, the uncoated PE cell short-circuited internally with severe thermal runaway (Fig. 6b), attributed to thermal shrinkage of the separator (Fig. 6c). Quantitative measurements at temperatures above 100 °C revealed negligible shrinkage for the W-PE and confirmed its enhanced thermal stability (Fig. 6d). Visual monitoring during thermal abuse testing revealed the stark difference: the W-PE cell maintained its structural integrity (Fig. 6e), whereas the uncoated PE cell experienced electrolyte vaporization and pouch rupture with gas evolution (Fig. 6f). These results indicate that the W-PE, particularly owing to the boehmite coating that prohibits thermal shrinkage, effectively overcomes the thermal stability challenges, a critical achievement for high-energy battery systems.[65] Thus, the strategically employed dual-side coating in our W-PE provides a comprehensive solution for LMBs by delivering both high performance and enhanced safety.

Conclusion

In summary, we introduced a novel interfacial engineering strategy that enables high-performance LMBs with enhanced safety through controlled Li metal densification. By exploiting the strong interfacial repulsion arising from the intrinsic immiscibility of W with Li, we achieved spontaneous Li metal

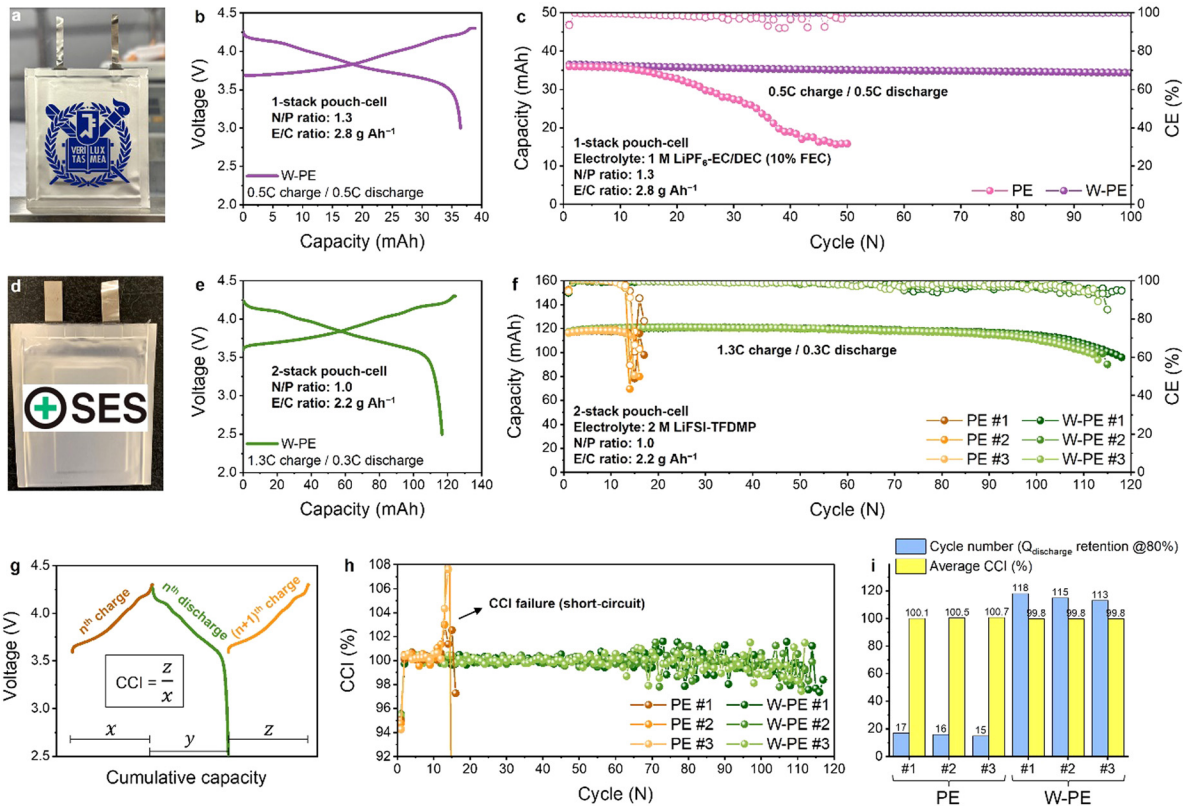

Fig. 5 Pouch-cell evaluations with limited Li metal and electrolyte resources. (a)–(c) Single-stack pouch-cell (36 mA h level) evaluations using a carbonate-based electrolyte (1 M $LiPF_6$ in EC/DEC with 10% FEC). (a) Photograph of the pouch-cell. (b) 1st voltage profile during 0.5C cycling. (c) Corresponding cycling performances. (d)–(f) Two-stack pouch-cell (118 mA h level) evaluations using an advanced electrolyte (2 M Li bis(fluorosulfonyl)imide (LiFSI) in 1,1,1-trifluoro-2,3-dimethoxypropane (TFDMP)). (d) Photograph of the pouch-cell. (e) 1st voltage profile during 1.3C/0.3C cycling. (f) Corresponding cycling performances across multiple cells. (g)–(i) Charge capacity increase (CCI) evaluations of the two-stack pouch-cells. (g) Illustration of the definition of CCI: ratio of the (n + 1)th charge capacity to the nth charge capacity. (h) Variation in CCI value during cycling. (i) Average CCI value and capacity retention across multiple cells.

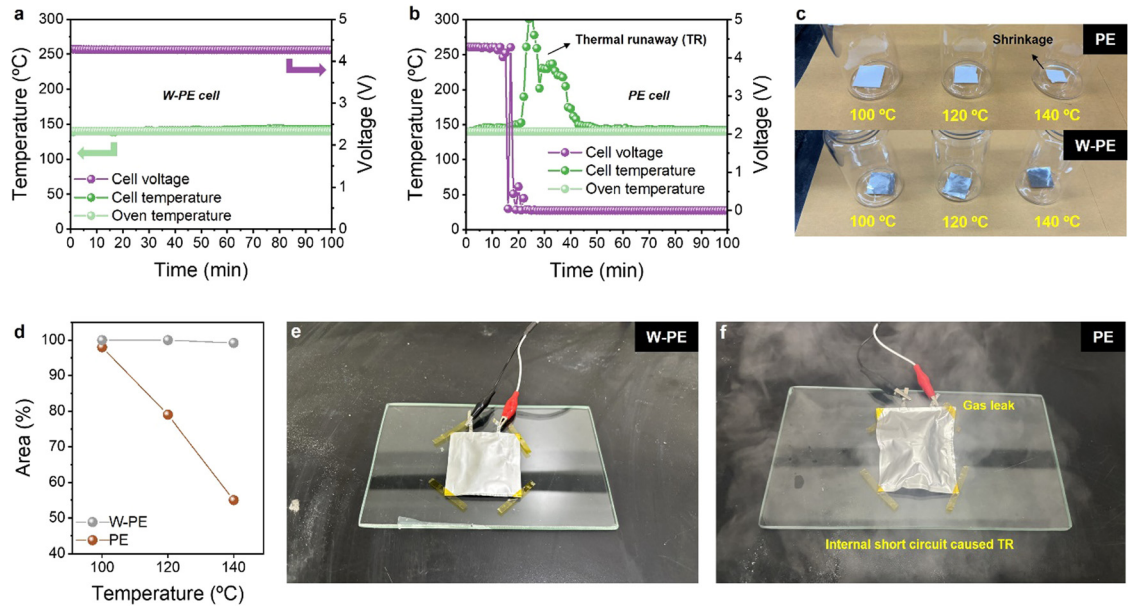

Fig. 6 Thermal runaway test under thermally abusive conditions. (a) and (b) Temperature and OCV monitoring of the pouch-cells at 140 °C and 100% SOC (4.3 V), using the (a) W-PE and (b) PE. (c) Photograph of the separators after exposure to elevated temperatures. (d) Shrinkage measurements of the separators after high-temperature treatment. (e) and (f) Photographs of the pouch-cells after the thermal runaway test for 50 minutes at 140 °C, using the (e) W-PE and (f) PE separators.

cohesion without additional processing requirements, such as protective coatings on the Li metal anode. The dual-sided coating scheme, which combines nanoscale W deposition with a boehmite coating, realized an ultrathin separator with a total thickness of merely 9 μm. This coating strategy effectively suppressed separator shrinkage at elevated temperatures to significantly suppress thermal runaway. Equally important, this strategy significantly improved the cycling and storage performance, even with a conventional carbonate-based electrolyte, to address the economic concerns associated with the use of complex electrolyte chemistries. Independent validation by SES AI Corporation under stringent conditions—limited Li metal and electrolyte resources, coupled with demanding fast-charge/slow-discharge protocols with high real-world demands—proved the commercial feasibility of our approach. Finally, because the proposed strategy does not require major modifications to existing LIB manufacturing processes, facile and immediate adoptability is warranted.

Author contributions

J. O. and J. W. C. conceived and designed the research. J. L. F. and R. A. L. fabricated and evaluated pouch-cells. H. K. performed DFT calculations. J. O., J. K., and M. K. conducted sample characterizations and electrochemical measurements. J. O. and J. W. C. co-wrote the manuscript. J. W. C. supervised the research. All authors participated in discussions of the results and commented on the manuscript.

Conflicts of interest

The authors filed a relevant patent application.

Data availability

The data supporting the findings of this study are available within the article and its ESI.† Additional datasets generated and analyzed during the current study are available from the corresponding author on reasonable request. No software or code have been included as part of this study.

Acknowledgements

J. W. C. acknowledges financial support from the Swiss National Science Foundation (SNF) (Sinergia CRSII5_202296) and the National Research Foundation of Korea (NRF) (RS-2024-00335274, RS-2024-00429941, and RS-2023-00261543). J. W. C. also acknowledges generous support from the Institute of Engineering Research (IOER), the Institute for Battery Research Innovation (IBRI), and the Research Institute of Advanced Materials (RIAM) at Seoul National University.

References

1 M. Armand and J. M. Tarascon, *Nature*, 2008, **451**, 652–657.
2 Z. P. Cano, D. Banham, S. Ye, A. Hintennach, J. Lu, M. Fowler and Z. Chen, *Nat. Energy*, 2018, **3**, 279–289.
3 J. W. Choi and D. Aurbach, *Nat. Rev. Mater.*, 2016, **1**, 16013.
4 C.-Y. Wang, T. Liu, X.-G. Yang, S. Ge, N. V. Stanley, E. S. Rountree, Y. Leng and B. D. McCarthy, *Nature*, 2022, **611**, 485–490.
5 V. A. Agubra and J. W. Fergus, *J. Power Sources*, 2014, **268**, 153–162.
6 C. Yang, J. Chen, X. Ji, T. P. Pollard, X. Lü, C.-J. Sun, S. Hou, Q. Liu, C. Liu, T. Qing, Y. Wang, O. Borodin, Y. Ren, K. Xu and C. Wang, *Nature*, 2019, **569**, 245–250.
7 C. K. Chan, H. Peng, G. Liu, K. McIlwrath, X. F. Zhang, R. A. Huggins and Y. Cui, *Nat. Nanotechnol.*, 2008, **3**, 31–35.
8 T. Lee, M. J. Seong, H. C. Ahn, M. Baek, K. Park, J. Oh, T. Choi and J. W. Choi, *Proc. Natl. Acad. Sci. U. S. A.*, 2025, **122**, e2417053121.
9 C. Fang, J. Li, M. Zhang, Y. Zhang, F. Yang, J. Z. Lee, M.-H. Lee, J. Alvarado, M. A. Schroeder, Y. Yang, B. Lu, N. Williams, M. Ceja, L. Yang, M. Cai, J. Gu, K. Xu, X. Wang and Y. S. Meng, *Nature*, 2019, **572**, 511–515.
10 J. Liu, Z. Bao, Y. Cui, E. J. Dufek, J. B. Goodenough, P. Khalifah, Q. Li, B. Y. Liaw, P. Liu, A. Manthiram, Y. S. Meng, V. R. Subramanian, M. F. Toney, V. V. Viswanathan, M. S. Whittingham, J. Xiao, W. Xu, J. Yang, X.-Q. Yang and J.-G. Zhang, *Nat. Energy*, 2019, **4**, 180–186.
11 A. J. Louli, A. Eldesoky, R. Weber, M. Genovese, M. Coon, J. deGooyer, Z. Deng, R. T. White, J. Lee, T. Rodgers, R. Petibon, S. Hy, S. J. H. Cheng and J. R. Dahn, *Nat. Energy*, 2020, **5**, 693–702.
12 N. Lee, J. Oh and J. W. Choi, *Mater. Futures*, 2023, **2**, 013502.
13 L. Braks, J. Zhang, A. Forster, P. Fritz, J. Oh, M. El Kazzi, J. W. Choi and A. Coskun, *Angew. Chem., Int. Ed.*, 2024, **63**, e202408238.
14 M. D. Tikekar, S. Choudhury, Z. Tu and L. A. Archer, *Nat. Energy*, 2016, **1**, 16114.
15 A. Jana, S. I. Woo, K. S. N. Vikrant and R. E. García, *Energy Environ. Sci.*, 2019, **12**, 3595–3607.
16 C. Niu, D. Liu, J. A. Lochala, C. S. Anderson, X. Cao, M. E. Gross, W. Xu, J.-G. Zhang, M. S. Whittingham, J. Xiao and J. Liu, *Nat. Energy*, 2021, **6**, 723–732.
17 Z. Yu, P. E. Rudnicki, Z. Zhang, Z. Huang, H. Celik, S. T. Oyakhire, Y. Chen, X. Kong, S. C. Kim, X. Xiao, H. Wang, Y. Zheng, G. A. Kamat, M. S. Kim, S. F. Bent, J. Qin, Y. Cui and Z. Bao, *Nat. Energy*, 2022, **7**, 94–106.
18 H. Wan, J. Xu and C. Wang, *Nat. Rev. Chem.*, 2024, **8**, 30–44.
19 S. Jiao, X. Ren, R. Cao, M. H. Engelhard, Y. Liu, D. Hu, D. Mei, J. Zheng, W. Zhao, Q. Li, N. Liu, B. D. Adams, C. Ma, J. Liu, J.-G. Zhang and W. Xu, *Nat. Energy*, 2018, **3**, 739–746.
20 Z. Yu, H. Wang, X. Kong, W. Huang, Y. Tsao, D. G. Mackanic, K. Wang, X. Wang, W. Huang, S. Choudhury, Y. Zheng, C. V. Amanchukwu, S. T. Hung, Y. Ma, E. G. Lomeli, J. Qin, Y. Cui and Z. Bao, *Nat. Energy*, 2020, **5**, 526–533.
21 J. Zheng, M. H. Engelhard, D. Mei, S. Jiao, B. J. Polzin, J.-G. Zhang and W. Xu, *Nat. Energy*, 2017, **2**, 17012.

22 H. Zhang, X. Liao, Y. Guan, Y. Xiang, M. Li, W. Zhang, X. Zhu, H. Ming, L. Lu, J. Qiu, Y. Huang, G. Cao, Y. Yang, L. Mai, Y. Zhao and H. Zhang, *Nat. Commun.*, 2018, **9**, 3729.
23 X. Liang, Q. Pang, I. R. Kochetkov, M. S. Sempere, H. Huang, X. Sun and L. F. Nazar, *Nat. Energy*, 2017, **2**, 17119.
24 X. Zhang, A. Wang, X. Liu and J. Luo, *Acc. Chem. Res.*, 2019, **52**, 3223–3232.
25 K. Yan, Z. Lu, H.-W. Lee, F. Xiong, P.-C. Hsu, Y. Li, J. Zhao, S. Chu and Y. Cui, *Nat. Energy*, 2016, **1**, 16010.
26 Y. Sohn, J. Oh, J. Lee, H. Kim, I. Hwang, G. Noh, T. Lee, J. Y. Kim, K. Y. Bae, T. Lee, N. Lee, W. J. Chung and J. W. Choi, *Adv. Mater.*, 2024, **36**, 2407443.
27 S. Zhouting, Z. Qihang, W. Zhenyu, C. Yifei, W. Kaiming, S. Fei, G. Juchen and H. Xiaogang, *Energy Mater.*, 2024, **4**, 400047.
28 X. Xiong, W. Yan, Y. Zhu, L. Liu, L. Fu, Y. Chen, N. Yu, Y. Wu, B. Wang and R. Xiao, *Adv. Energy Mater.*, 2022, **12**, 2103112.
29 Z. Wu, C. Wang, Z. Hui, H. Liu, S. Wang, S. Yu, X. Xing, J. Holoubek, Q. Miao, H. L. Xin and P. Liu, *Nat. Energy*, 2023, **8**, 340–350.
30 X. Feng, M. Ouyang, X. Liu, L. Lu, Y. Xia and X. He, *Energy Storage Mater.*, 2018, **10**, 246–267.
31 D. P. Finegan, M. Scheel, J. B. Robinson, B. Tjaden, I. Hunt, T. J. Mason, J. Millichamp, M. Di Michiel, G. J. Offer, G. Hinds, D. J. L. Brett and P. R. Shearing, *Nat. Commun.*, 2015, **6**, 6924.
32 X. Wang, W. Zeng, L. Hong, W. Xu, H. Yang, F. Wang, H. Duan, M. Tang and H. Jiang, *Nat. Energy*, 2018, **3**, 227–235.
33 M. Kim, J. An, S.-J. Shin, I. Hwang, J. Lee, Y. Park, J. Kim, E. Park, J. Kim, G. Park, S. Kim, A. Coskun and J. W. Choi, *Energy Environ. Sci.*, 2024, **17**, 6079–6090.
34 L. Qiao, U. Oteo, M. Martinez-Ibañez, A. Santiago, R. Cid, E. Sanchez-Diez, E. Lobato, L. Meabe, M. Armand and H. Zhang, *Nat. Mater.*, 2022, **21**, 455–462.
35 Z. Yang, Y. Zhu, X. Tan, S. J. J. Gunjal, P. Dewapriya, Y. Wang, R. Xin, C. Fu, K. Liu, K. Macintosh, L. G. Sprague, L. Leung, T. E. Hopkins, K. V. Thomas, J. Guo, A. K. Whittaker and C. Zhang, *Nat. Commun.*, 2024, **15**, 8269.
36 H. Kwon, H. Kim, J. Hwang, W. Oh, Y. Roh, D. Shin and H.-T. Kim, *Nat. Energy*, 2024, **9**, 57–69.
37 J. Oh, S. H. Choi, H. Kim, J. Y. Kim, G.-J. Lee, K. Y. Bae, T. Lee, N. Lee, Y. Sohn, W. J. Chung and J. W. Choi, *Energy Environ. Sci.*, 2024, **17**, 7932–7943.
38 J. Sangster and A. D. Pelton, *J. Phase Equilib.*, 1991, **12**, 203.
39 X. Fan, X. Ji, F. Han, J. Yue, J. Chen, L. Chen, T. Deng, J. Jiang and C. Wang, *Sci. Adv.*, 2018, **4**, eaau9245.
40 Y. Liu, X. Tao, Y. Wang, C. Jiang, C. Ma, O. Sheng, G. Lu and X. W. Lou, *Science*, 2022, **375**, 739–745.
41 J. Chen, X. Fan, Q. Li, H. Yang, M. R. Khoshi, Y. Xu, S. Hwang, L. Chen, X. Ji, C. Yang, H. He, C. Wang, E. Garfunkel, D. Su, O. Borodin and C. Wang, *Nat. Energy*, 2020, **5**, 386–397.
42 Z. Piao, R. Gao, Y. Liu, G. Zhou and H.-M. Cheng, *Adv. Mater.*, 2023, **35**, 2206009.
43 N. Piao, S. Liu, B. Zhang, X. Ji, X. Fan, L. Wang, P.-F. Wang, T. Jin, S.-C. Liou, H. Yang, J. Jiang, K. Xu, M. A. Schroeder, X. He and C. Wang, *ACS Energy Lett.*, 2021, **6**, 1839–1848.
44 C. Yang, Y. Yao, S. He, H. Xie, E. Hitz and L. Hu, *Adv. Mater.*, 2017, **29**, 1702714.
45 J. Oh, S. H. Choi, B. Chang, J. Lee, T. Lee, N. Lee, H. Kim, Y. Kim, G. Im, S. Lee and J. W. Choi, *ACS Energy Lett.*, 2022, **7**, 1374–1382.
46 J. Oh, D. Kwon, S. H. Choi, N. Lee, Y. Sohn, T. Lee, T. Lee, J. Y. Kim, K. Y. Bae and J. W. Choi, *Adv. Energy Mater.*, 2025, **15**, 2404817.
47 N. Lee, J. Lee, T. Lee, J. Oh, I. Hwang, G. Seo, H. Kim and J. W. Choi, *ACS Appl. Mater. Interfaces*, 2023, **15**, 34931–34940.
48 C. Yang, H. Tong, C. Luo, S. Yuan, G. Chen and Y. Yang, *J. Power Sources*, 2017, **348**, 80–86.
49 R. Qiao, Y. Zhao, S. Zhou, H. Zhang, F. Liu, T. Zhou, B. Sun, H. Fan, C. Li, Y. Zhang, F. Liu, X. Ding, J. Wook Choi, A. Coskun and J. Song, *Chemistry*, 2024, **11**, 102306.
50 A.-M. Li, O. Borodin, T. P. Pollard, W. Zhang, N. Zhang, S. Tan, F. Chen, C. Jayawardana, B. L. Lucht, E. Hu, X.-Q. Yang and C. Wang, *Nat. Chem.*, 2024, **16**, 922–929.
51 C. M. Efaw, Q. Wu, N. Gao, Y. Zhang, H. Zhu, K. Gering, M. F. Hurley, H. Xiong, E. Hu, X. Cao, W. Xu, J.-G. Zhang, E. J. Dufek, J. Xiao, X.-Q. Yang, J. Liu, Y. Qi and B. Li, *Nat. Mater.*, 2023, **22**, 1531–1539.
52 Y. Yamada, J. Wang, S. Ko, E. Watanabe and A. Yamada, *Nat. Energy*, 2019, **4**, 269–280.
53 C. Ding, Y. Liu, L. K. Ono, G. Tong, C. Zhang, J. Zhang, J. Lan, Y. Yu, B. Chen and Y. B. Qi, *Energy Storage Mater.*, 2022, **50**, 417–425.
54 D. Luo, L. Zheng, Z. Zhang, M. Li, Z. Chen, R. Cui, Y. Shen, G. Li, R. Feng, S. Zhang, G. Jiang, L. Chen, A. Yu and X. Wang, *Nat. Commun.*, 2021, **12**, 186.
55 J. Zheng, P. Yan, D. Mei, M. H. Engelhard, S. S. Cartmell, B. J. Polzin, C. Wang, J.-G. Zhang and W. Xu, *Adv. Energy Mater.*, 2016, **6**, 1502151.
56 Y. Zhao, T. Zhou, M. Mensi, J. W. Choi and A. Coskun, *Nat. Commun.*, 2023, **14**, 299.
57 X.-Q. Zhang, T. Li, B.-Q. Li, R. Zhang, P. Shi, C. Yan, J.-Q. Huang and Q. Zhang, *Angew. Chem., Int. Ed.*, 2020, **59**, 3252–3257.
58 C. Niu, H. Pan, W. Xu, J. Xiao, J.-G. Zhang, L. Luo, C. Wang, D. Mei, J. Meng, X. Wang, Z. Liu, L. Mai and J. Liu, *Nat. Nanotechnol.*, 2019, **14**, 594–601.
59 P. Shi, X.-Q. Zhang, X. Shen, B.-Q. Li, R. Zhang, L.-P. Hou and Q. Zhang, *Adv. Funct. Mater.*, 2021, **31**, 2004189.
60 Y. Gao, M. Guo, K. Yuan, C. Shen, Z. Ren, K. Zhang, H. Zhao, F. Qiao, J. Gu, Y. Qi, K. Xie and B. Wei, *Adv. Energy Mater.*, 2020, **10**, 1903362.
61 C. Niu, H. Lee, S. Chen, Q. Li, J. Du, W. Xu, J.-G. Zhang, M. S. Whittingham, J. Xiao and J. Liu, *Nat. Energy*, 2019, **4**, 551–559.
62 P. Zhao, Y. Li, S. Chen, H. Fan, Y. Feng, L. Hu, Y. Zhang, Q. Nie, H. Pei, C. Yang, J. Deng, C. Bao and J. Song, *Adv. Energy Mater.*, 2022, **12**, 2200568.
63 W. Deng, W. Dai, X. Zhou, Q. Han, W. Fang, N. Dong, B. He and Z. Liu, *ACS Energy Lett.*, 2021, **6**, 115–123.
64 Y. Liu, Y. Zhu and Y. Cui, *Nat. Energy*, 2019, **4**, 540–550.
65 X. Zhang, L. Huang, B. Xie, S. Zhang, Z. Jiang, G. Xu, J. Li and G. Cui, *Adv. Energy Mater.*, 2023, **13**, 2203648.